ACS APPLIED MATERIALS & INTERFACES

www.acsami.org

Research Article

Hydrothermal Surface Engineering of Anodic WO_3 Photoelectrode by Simultaneous Iron Doping and $Fe_3O_4/FeWO_4$ Formation

Piyali Chatterjee,* Daniel Piecha, Sebastian Kotarba, Karolina Syrek, Marcin Pisarek, and Grzegorz D. Sulka*

Cite This: *ACS Appl. Mater. Interfaces* 2025, 17, 30284−30296

Read Online

ACCESS | Metrics & More | Article Recommendations | Supporting Information

ABSTRACT: This study reports a hydrothermal surface modification approach to porous anodized WO_3 to enhance its photoelectrochemical water oxidation performance. This results in the Fe doping of monoclinic WO_3 and the simultaneous formation of Fe-containing phases, such as $FeWO_4$ and Fe_3O_4. The photocurrent generated at the surface-engineered electrodes was double that of pure WO_3 with long-term stability. The enhancement is attributable to the creation of oxygen vacancies due to Fe doping and the formation of the heterojunction between WO_3 and $FeWO_4$, a p-type semiconductor, which likely improved the charge carrier lifetime and charge transfer properties. Incident photon to current efficiency (IPCE) measurements revealed enhanced visible light performance, supported by the observed red shift in the light absorption edge. This work is one of the few explorations of WO_3 photoanodes with an opaque metal substrate that involves fabrication of a light-facing overlayer at the surface. Characterization of the fabricated electrodes was carried out using X-ray diffraction (XRD), scanning electron microscopy (FESEM), energy dispersive X-ray spectroscopy (EDS), X-ray photoelectron spectroscopy (XPS), Raman spectroscopy, and diffuse reflectance spectroscopy (UV−Vis DRS). Photoelectrochemical studies were conducted using linear voltammetry, amperometry, and electrochemical impedance spectroscopy (Nyquist, Bode, and Mott−Schottky plots).

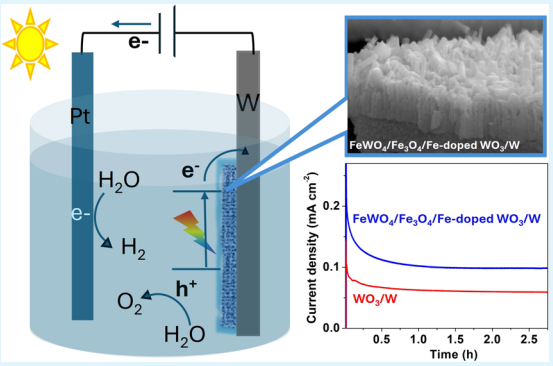

KEYWORDS: *photoelectrochemical, photoanode, anodic oxidation, tungsten oxide, water splitting, hydrothermal*

1. INTRODUCTION

The abundant yet intermittent nature of sunlight necessitates efficient energy conversion and storage mechanisms, with water photoelectrocatalysis for producing portable green hydrogen emerging as a popular solution. A primary challenge in solar water splitting research is the sluggish kinetics of the water oxidation reaction at a photoanode surface, prompting the exploration of numerous efficient materials since the pioneering studies on wide band gap TiO_2.[1,2] In photoelectrochemical water splitting, the same material often serves as both the light-absorbing and gas-evolving surface, requiring it to fulfill multiple demanding criteria. Tungsten oxide is a visible light-active, moderate band gap (~2.7 eV) n-type semiconductor that offers notable advantages, including stability in acidic media, a relatively long (compared to Fe_2O_3 for example) hole diffusion length (~150 nm), and a valence band maximum positioned favorably below the water oxidation potential.[3,4] Despite these benefits, WO_3 is susceptible to photocorrosion and has a low absorption coefficient, requiring the use of thicker layers, which increases the risk of unwanted recombination of photogenerated charge carriers. The challenges associated with charge transfer at the substrate/semiconductor interface can be significantly mitigated by directly growing highly crystalline, porous semiconductors on conducting substrates.[5,6] Doping metal oxides with metal cations improves light absorption, electrical conductivity, and catalytic properties, and is also common in the existing literature on WO_3 for solar water splitting.[7−9]

To further enhance performance, electrocatalysts grown/deposited on the surface often serve as a suitable co-catalyst for the photoabsorbing primary semiconductor photocatalyst. The electrocatalyst increases the production rate, while the photocatalyst reduces the potential required for electrolysis.[10] Such surface engineering, particularly when aimed at creating heterojunctions, introduces new interfaces that can potentially hinder the efficient transport of photogenerated charge carriers. However, this challenge can be mitigated through semiconductor doping, which modifies the band gap and/or reduces the material's ohmic resistance.[7,11] Alternatively,

Received: February 18, 2025
Revised: May 1, 2025
Accepted: May 1, 2025
Published: May 8, 2025

forming a heterojunction with a material or catalyst that beneficially alters surface chemistry and/or enhances conductivity offers another viable strategy.[12] Notably, WO_3/Fe_3O_4 heterojunction have been reported to function efficiently as photocatalysts, where Fe_3O_4 sensitizes WO_3 and extends its visible light absorption range.[13,14] If the conduction and valence band edges of the primary electrode material and the co-catalyst are aligned properly, electron−hole separation is facilitated by the timely transfer of electrons from the anode toward the cathode and holes to water. Incorporating p-type or ferroelectric semiconductors (e.g., $CoWO_4$, $CaFe_2O_4$, Fe_3O_4, $FeWO_4$, etc.) with n-type semiconductors (Fe_2O_3, WO_3, and $BiVO_4$) can therefore aid the process by utilizing their built-in potential to drive charge separation.[15−20] Interestingly, various transition metal tungstates have been previously reported in composites or heterojunctions with WO_3 due to their similar crystalline structures, particularly the shared chains of WO_6 groups. Tungstates are chemically robust and offer surface protective roles too.[21−29] For instance, Zhu et al. demonstrated ∼1.6 times higher photocurrent from a $NiWO_4/WO_3$ heterostructure on FTO glass compared to WO_3 alone.[21] Another study also showed performance enhancement using $NiWO_4$- and $CuWO_4$-modified WO_3 on FTO glass.[25] Li et al. reported a photocurrent 5.6 times higher and more stable than that of pristine WO_3 for hydrothermally grown WO_3 modified by electrodeposited $CuWO_4/CuO$, where p-type CuO acts as a light sensitizer and $CuWO_4$ aids in charge separation.[28] In another study, a 2-fold increase in photocurrent was observed after a multistep Fe-based modification ($FeOOH/Fe_2WO_6$/Fe doping) of hydrothermally grown WO_3 on FTO glass.[29] Additionally, $FeWO_4$ (E_g ∼ 2.0 eV), either pure or containing Fe oxides, has been studied in composites with n-type WO_3 and WO_x for applications such as photocatalytic organic pollutant degradation, sensing, and electrocatalytic water splitting.[30−34] However, despite theoretical predictions suggesting its potential,[35] the electrocatalytic nature of $FeWO_4$ has not yet been utilized as a co-catalyst for WO_3 photoanodes.[36]

Among various WO_3 fabrication techniques, anodic oxidation stands out as a highly reproducible and scalable method, where a metal substrate surface is directly converted into the corresponding metal oxide. This process ensures that the oxide layer is strongly adhered to the current collector (metal substrate), resulting in lower interfacial resistances compared to deposition-based electrodes.[37] This advantage is often underexplored,[38] especially when compared to widely used transparent conductive glass substrates, where materials are coated or grown on the surface of photoelectrodes.

The opaque nature of the metal substrate in any anodized electrode makes front illumination necessary, and thus only a thin and dispersed overlayer may be made to function in a beneficial way, avoiding shading of the WO_3 underneath. This is important especially if the overlayer material's band gap is comparable to WO_3. Therefore, while extensive studies have focused on pure or doped anodic WO_3 photoanodes,[37,39,40] very limited literature exists on co-catalyst-modified anodic WO_3.[23,38,41] To address this gap, we aimed to fabricate $FeWO_4$ on anodic WO_3 using hydrothermal method,[30,42] with the goal of improving efficiency and reducing corrosion of underlying WO_3. Although hydrothermal synthesis is relatively slow, it offers superior phase control and morphological uniformity compared with other simple wet-chemical methods by tuning parameters such as temperature, time, and solvent. This method allows for the formation of well-crystallized products with moderate scalability, low cost, and operation at moderate temperatures.[43,44]

Generally, doping during anodization requires addition of the dopant precursor in electrolyte or using bimetallic alloys and thus may involve a risk of unwanted defects in the formation of the intended oxide phase. However, our hydrothermal technique can proceed on any pure WO_3 synthesis route. It is also interesting that our treatment resulted in formation of $FeWO_4−Fe_3O_4$ phases and simultaneously doped WO_3 with Fe at the same step.[11] Notable improvements in photocurrent at low bias and in the visible light range were observed compared to that in pristine WO_3. These enhancements were correlated with results from X-ray diffraction, X-ray photoelectron spectroscopy, Raman spectroscopy, electrochemical impedance spectroscopy, and changes in the indirect band gap values. To the best of our knowledge, there is no prior report on the use of a hydrothermal technique to engineer the surface of anodic WO_3 photoelectrodes for better performance.

2. EXPERIMENTAL SECTION

2.1. Materials. W metal foil (Goodfellow, 0.2 mm thick, 99.95%), ammonium sulfate ($(NH_4)_2SO_4$, > 99%, Sigma-Aldrich), ammonium fluoride (NH_4F, < 99%, Merck), Mohr's salt/ammonium iron sulfate hexahydrate ($(NH_4)_2SO_4·Fe(SO_4)·6H_2O$, > 99%, Thermo Scientific), iron(II) sulfate heptahydrate ($FeSO_4·7H_2O$, > 99%, Sigma-Aldrich), iron(III) chloride ($FeCl_3$, > 99%, Sigma), 25% ammonia (NH_3, Chempur), hydrofluoric acid (HF, 40%, Merck), iron(II) chloride tetrahydrate ($FeCl_2·4H_2O$, > 99%, Sigma-Aldrich), sodium hydroxide (NaOH, 98.8%, Chempur), and sodium sulfate (Na_2SO_4 > 99%, Sigma-Aldrich) were used without further purification.

2.1.1. Synthesis of WO_3. WO_3 was synthesized via anodic oxidation in a two-electrode setup, comprising a W foil (cleaned with ethanol/acetone) as the anode and a Pt wire grid as the cathode (larger than the active area of the anode) positioned 2 cm apart. The W foil was cut into 2 × 1 cm^2 pieces, and insulating paint was applied, leaving an exposed area of ∼0.5 cm^2 to define the active area. An aqueous solution of 1 M $(NH_4)_2SO_4$ and 75 mM NH_4F was stirred continuously at 20 °C, while a constant voltage of 60 V was applied for 60 min.[45] After anodization, the electrodes were rinsed three times with deionized (DI) water. Next, the samples were etched in 20% HF at 30 °C under ultrasonication for 15 s, followed by a 5 s rinse in ethanol. The insulating paint was peeled off, and the electrodes were subsequently heated to 500 °C at a rate of 2 °C·min^{-1} in an air muffle furnace and annealed for 2 h. Finally, the samples were allowed to cool naturally to room temperature and stored for future use.[38] These samples are referred to as WO_3.

2.1.2. Surface Modification of WO_3. The annealed WO_3 electrodes were wrapped with Teflon tape around the edges to maintain a surface metallic for terminals. The samples were clamped and immersed in a beaker containing 30 mL of an aqueous 0.125 mM Mohr's salt ($(NH_4)_2SO_4·Fe(SO_4)·6H_2O$) solution (pH = 5.4) under continuous stirring. To adjust the pH, a 25% ammonia (NH_3) solution was added rapidly, raising the pH to ∼ 8.3. Stirring was maintained for about 45 min, during which the pH came down to ∼8.0. The solution was then transferred to a sealed 50 mL Teflon-lined chamber within a stainless steel autoclave. The electrodes were placed inside in an inclined position, with the WO_3 surface facing upward to prevent excessive deposition. Hydrothermal treatment was conducted at 180 °C for 6 h in a hot air oven. After slow cooling, the pH of the medium was measured to be ∼ 5.0. The electrodes were rinsed with DI water, air-dried, and annealed at 500 °C for 2 h. These samples, termed WO_3/NH_3/Fe, exhibited the best photoelectrochemical performance. A schematic of the procedure is provided in Figure S1 (Supporting Information) along with a possible reaction pathway for $FeWO_4$ formation (eqs S1 and S2), provided the thermodynamic conditions are suitable. To give an idea of the optimization of the surface

https://doi.org/10.1021/acsami.5c03437
ACS Appl. Mater. Interfaces 2025, 17, 30284−30296

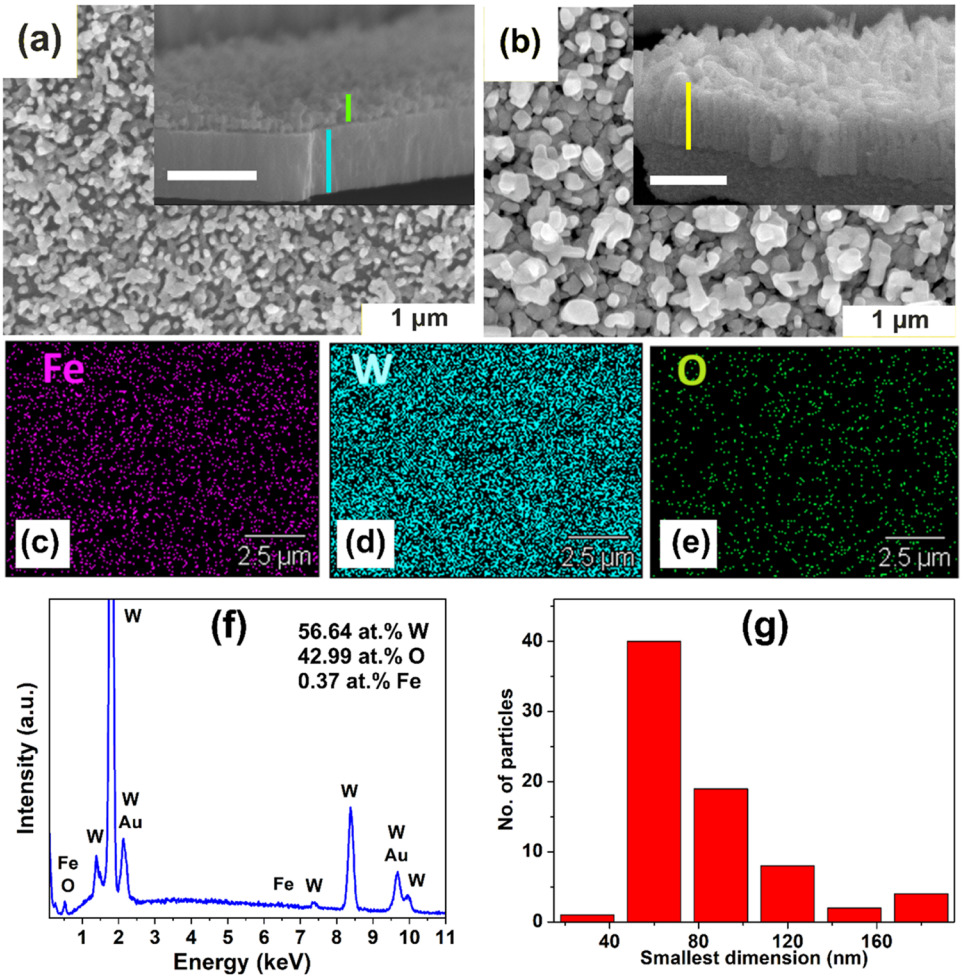

Figure 1. FESEM images of (a) WO_3 (top view) and (inset) its cross-sectional view with 1 μm scale bar. (b) WO_3/NH_3/Fe (top view) and (inset) its cross-sectional view with 1 μm scale bar. (c–e) Representative elemental mapping for Fe, W, and O on the WO_3/NH_3/Fe electrode surface. (f) Corresponding areal EDS spectrum for a WO_3/NH_3/Fe sample. (g) Particle size histogram of WO_3/NH_3/Fe.

treatment route described above, we provided in Supporting Information some results from WO_3 samples which were also modified using a similar method but with specific variations, as listed below: (a) replacement of 25% NH_3 with 1 M NaOH, (b) annealing in vacuum instead of air, (c) use of 25% NH_3 solution alone without the addition of Fe precursor, (d) substitution of Mohr's salt with 0.125 mM $FeCl_3$, $FeCl_2$, or $FeSO_4$, and (e) adjustment of the Mohr's salt concentration from 0.125 to 0.063, 0.25, and 0.5 mM. A summary of all hydrothermal synthesis conditions and their corresponding sample labels is provided in Table S1 (Supporting Information). Preliminary trials indicated that an alkaline pH promotes the formation of smaller particles during synthesis from the Mohr's salt; therefore, pH 8 was maintained for all samples presented in this work.

2.1.3. Characterization Techniques. Field emission scanning electron microscopy (FESEM) images were obtained by using a Hitachi S-4700 microscope equipped with an X-ray detector for energy dispersive spectroscopy (EDS, Thermo Noran System 7), operated at an acceleration voltage of 20 kV. The samples were sputter-coated with Au using a sputter current of 10 mA for 120 s, without any precleaning step. The corresponding FESEM images were analyzed by using ImageJ software. The UV–visible diffuse reflectance spectroscopy (UV–Vis DRS) was performed in the 200–800 nm wavelength range using a PerkinElmer Lambda 750S spectrophotometer. X-ray powder diffraction (XRD) measurements were carried out on a Malvern Panalytical Aeris diffractometer in the 2θ range of 10°-80°, with a step size of 0.02° and a scan rate of 2.8° min^{-1}. Cu Kα radiation (1.54 Å) was employed during acquisition with operating conditions set at 40 kV and 15 mA. X-ray photoelectron spectroscopy (XPS) was conducted on a Microlab350 spectrometer with a 20 W X-ray gun and an Al X-ray source (1486.6 eV). XPS spectra were analyzed using Thermo Avantage software (version 5.9911, Thermo Fisher Scientific), with the C 1s adventitious carbon peak at 284.6 eV used as a reference. A Horiba Xplora Plus Raman microscope with an incident laser of 532 nm wavelength operating at low intensity (1% of nominal 100 mW power) was used for Raman measurements. The laser beam was focused on the sample using a 100× objective (Olympus MPlan N, N_A = 0.9). Raman wavenumber shifts in the range of 0–1200 cm^{-1} were recorded. All photoelectrochemical studies, except impedance vs potential measurements (Mott–Schottky plots), were performed using a PalmSens4 potentiostat and a Teflon-based three-electrode cell with a quartz glass window. Mott–Schottky measurements were carried out using a Biologic SP-300 or VMP-300 potentiostat. The counter and reference electrodes were a platinum foil and saturated calomel electrode (SCE), respectively. The separation distances between the three electrodes were kept nearly constant.

A 0.1 M Na_2SO_4 solution was used as the electrolyte in all experiments, as both $FeWO_4$ and WO_3 are fairly stable at pH < 7. Linear sweep voltammetry (LSV) curves were recorded at a slow scan rate (5 mV s^{-1}) to minimize the capacitive dark current. The measurements were conducted under chopped illumination with 5 s on–off cycles. The potential window ranged from just below the onset potential to beyond the water oxidation potential at 1.23 V vs RHE (~0.6 V vs SCE). The Nernst equation used for the conversion from the SCE to RHE scale is given in eq S3 of Supporting Information. Nyquist plots were derived from electrochemical

https://doi.org/10.1021/acsami.5c03437
ACS Appl. Mater. Interfaces 2025, 17, 30284–30296

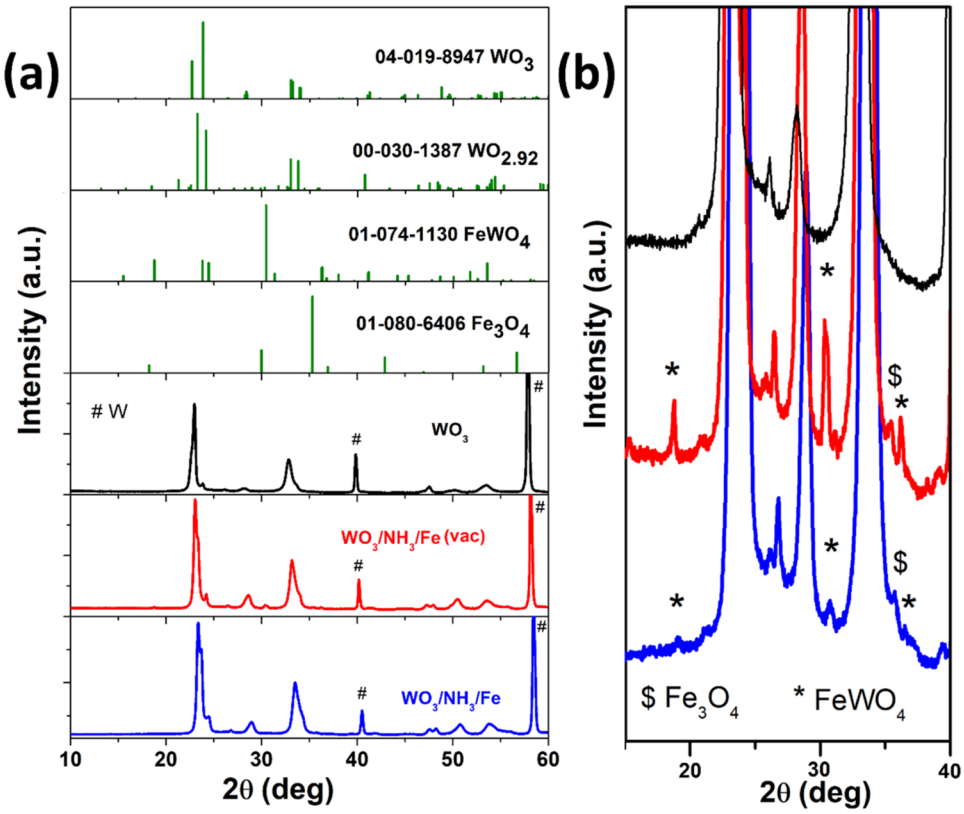

Figure 2. (a) X-ray diffractograms of pristine WO_3 along with hydrothermally modified $WO_3/NH_3/Fe$ and $WO_3/NH_3/Fe$ (vac) samples, in comparison to standard PDF5+ database patterns. (b) Stacked and intensity expanded diffractograms of WO_3, $WO_3/NH_3/Fe$ (vac), and $WO_3/NH_3/Fe$ in the 15−40° range.

impedance spectroscopy (EIS) measurements conducted over a frequency range of 0.1 Hz - 100 kHz with a 10 mV AC amplitude. Solar simulated illumination at 100 mW cm^{-2} power was provided by a 150 W Xe arc lamp (Instytut Fotonowy, Poland). Charge separation and charge injection efficiencies were measured by adding 0.1 M Na_2SO_3 to 0.1 M Na_2SO_4. The incident photon to current efficiency (IPCE) measurements were performed using a specialized photoelectric spectrometer equipped with a monochromator (Instytut Fotonowy, Poland). The IPCE plots were derived from photocurrent data recorded at 1.2 V vs RHE, using monochromatic light with a stepwise increase of 10 nm in the wavelength range of 300−480 nm.

3. RESULTS AND DISCUSSION

The initial stage of the research involved the selection of the best hydrothermal modification route for anodic WO_3 which has been discussed to some extent in the Supporting Information. Figures S2 and S3 (Supporting Information) present the top-view morphology of anodic WO_3 samples modified under various hydrothermal reaction parameters and an annealing atmosphere. The fabricated photoanodes were tested in the three-electrode configuration to compare their photoelectrochemical performances (see Figure S4, Supporting Information) and thus optimize the hydrothermal surface engineering protocol.

The top surface of pristine porous anodic WO_3 is shown in Figure 1a, which represents a typical morphology formed by the anodization method employed.[45] The cross-sectional view of this electrode, provided in the inset, distinctly shows the anodic layer (marked green) and the thermally oxidized layer (marked blue) of WO_3, with measured thicknesses of about 300 and 700 nm, respectively, across different samples. Figure 1b displays a top view of the $WO_3/NH_3/Fe$ sample, revealing an irregular plate-like morphology. This morphology is better understood in the lateral view in the inset showing plates of width <70 nm. A comparison of the two cross-section images highlights the significant transformation of the anodic WO_3 layer into $WO_3/NH_3/Fe$. Despite this transformation, the total height (marked yellow) of the structure above the tungsten substrate remains comparable to that of pristine WO_3.

Figure 1c−e shows the elemental mapping of $WO_3/NH_3/Fe$ obtained by EDS, revealing a mostly uniform coverage of the WO_3 surface with Fe. As expected, the EDS spectra in Figure 1f show the presence of W and O, along with Au (from sputter coating) and trace amounts of Fe. The absence of any noticeable N or S signal from the precursors used indicates a clean synthesis procedure. The stoichiometric 1:3 ratio (or at least a higher at.% of O compared to W) in WO_3 is not observed, which is understandable due to the presence of metallic W beneath the anodic oxide layers. The average Fe:W atomic ratio is ∼1% in all samples, indicating very dispersed incorporation of Fe on or within WO_3, as desirable. Figure 1g shows the particle size histogram of $WO_3/NH_3/Fe$. It indicates that the median length of the smallest dimension observed in the top view of the particles on the $WO_3/NH_3/Fe$ surface is 56 nm, while the mean length is 69 nm.

The X-ray diffractograms for the optimized samples annealed in air ($WO_3/NH_3/Fe$) and in vacuum ($WO_3/NH_3/Fe$ (vac)) are plotted in Figure 2a along with that of pristine WO_3 and standard reference databases for comparison. The sharp peaks observed at 2θ = 40.5, 58.5, and 73.4° are attributed to the cubic W foil substrate, corresponding to the (110), (200), and (211) planes, as matched with PDF card no. 00-001-1203. For WO_3, the major peaks observed are

https://doi.org/10.1021/acsami.5c03437
ACS Appl. Mater. Interfaces 2025, 17, 30284−30296

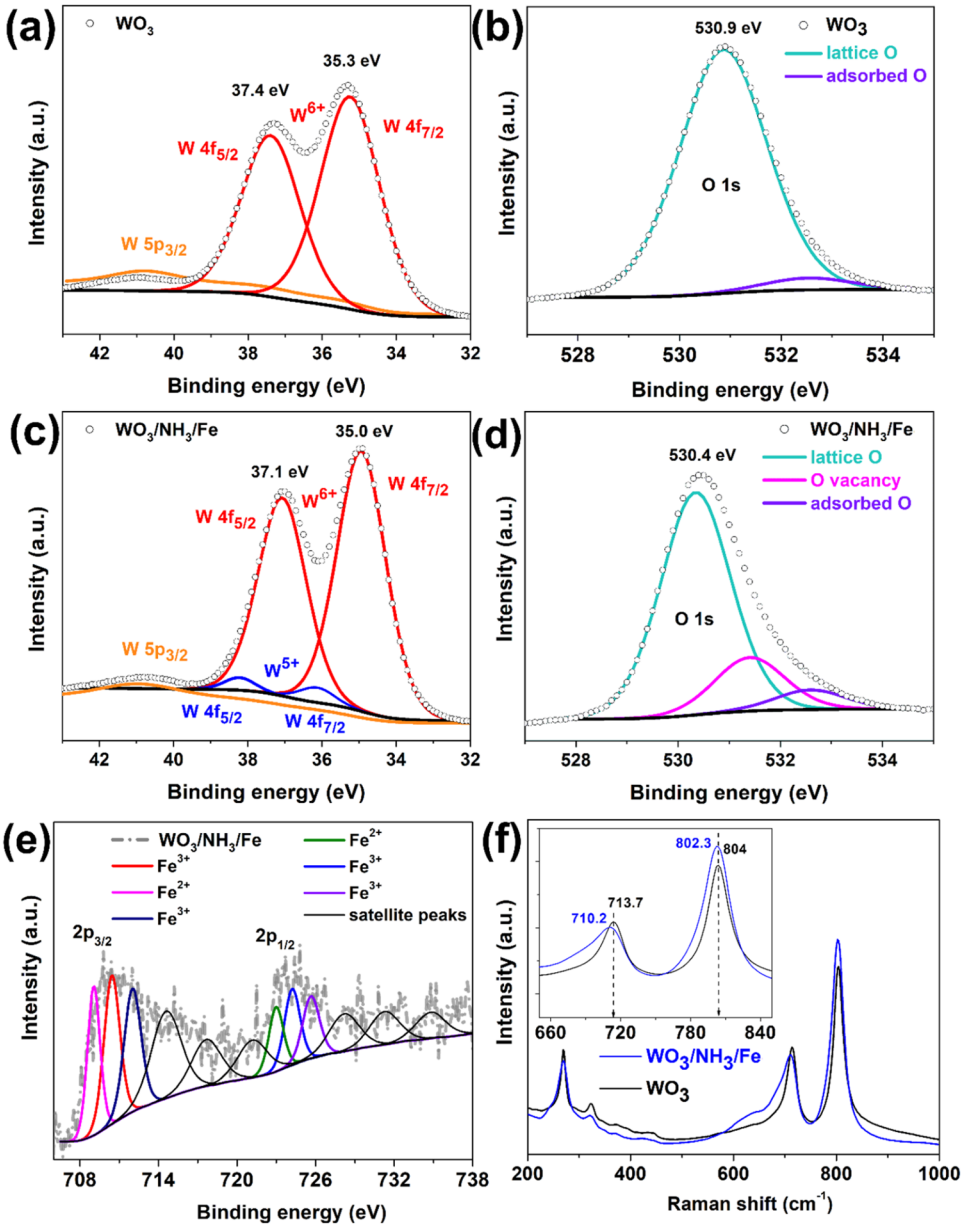

Figure 3. (a, b) High-resolution XPS spectra of WO_3 for (a) W 4f and (b) O 1s. (c–e) High-resolution XPS spectra of $WO_3/NH_3/Fe$ for (c) W 4f, (d) O 1s, and (e) Fe 2p. (f) Raman spectra of WO_3 and $WO_3/NH_3/Fe$.

characteristic of the stoichiometric monoclinic WO_3 phase (PDF card no. 04-019-8947). For $WO_3/NH_3/Fe$, all of the major peaks corresponding to another monoclinic phase (PDF card no. 00-030-1387) can also be identified. This phase has the empirical formula $WO_{2.92}$ and is one of the tungsten oxide polymorphs.[46] For doping WO_3 by Fe^{2+} precursor, a slight shift of the most intense stoichiometric WO_3 peak to higher angle has been found in literature as has also happened in our case (~0.4° shift).[47] Since the W:O stoichiometry is not identical across these anodic oxide materials, the observed shift can only be partially attributed to the slightly smaller covalent radius of Fe compared to W. Fe doping likely causes a contraction of the WO_3 lattice parameters, which, in turn, leads to a shift in peak positions according to Bragg's law of diffraction, along with changes in peak intensity ratios. For example, the ratio of the peak heights at ~23 and 24° decreases from 9.3 in pristine WO_3 to 6.2 in the $WO_3/NH_3/Fe$ sample.[48,49] However, very prominent shifts of the maxima of the most intense peak of WO_3 cannot be expected even for Fe doping in $WO_3/NH_3/Fe$, due to the similar ionic radii of W^{6+} (0.62 nm) and the Fe ions (Fe^{4+} – 0.39 nm, Fe^{3+} – 0.64 nm, Fe^{2+} – 0.77 nm).[50] In the expanded plot in Figure 2b, minor peaks at 2θ = 30.7, 19.0, and 36.5° correspond to the (111), (100), and (021) planes of monoclinic $FeWO_4$ (PDF card no. 01-074-1130), while the peak at 35.6° may originate from the most intense reflection of Fe_3O_4 (PDF card no. 01-080-6406). The peaks corresponding to $FeWO_4$ are more intense and easily identifiable for the vacuum-annealed $WO_3/NH_3/Fe$ (vac) sample and $FeWO_4$ appears to have undergone partial oxidative decomposition when annealed in air. The average crystallite size of $FeWO_4$ nanoparticles in the overlayer is estimated to be 18 nm, as calculated using the Debye–Scherrer equation (eq S4, Supporting Information).[49]

https://doi.org/10.1021/acsami.5c03437
ACS Appl. Mater. Interfaces 2025, 17, 30284–30296

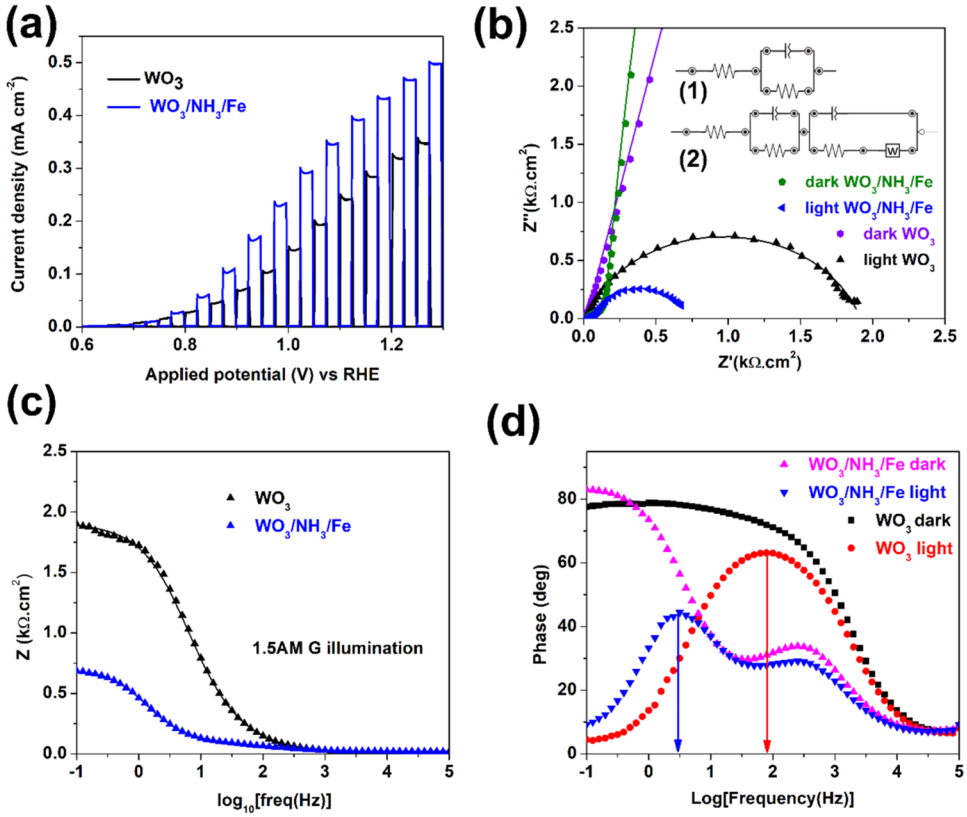

Figure 4. (a) Chopped LSVs under 1.5 AM G illumination for WO_3 and $WO_3/NH_3/Fe$. (b) Nyquist plots for the electrodes in the dark and under illumination (1.5 AM G) at 1.0 V vs RHE bias. Symbols depict experimental data and solid line curves follow the fitted data. Inset shows the equivalent circuit model for (1) WO_3 and (2) $WO_3/NH_3/Fe$. (c) Bode impedance plot under illumination and (d) Bode phase plots recorded in the dark and under illumination for WO_3 and $WO_3/NH_3/Fe$ at 1.0 V vs RHE.

X-ray photoelectron spectroscopy was used to investigate the surface changes in WO_3 after hydrothermal treatment. The high-resolution W 4f spectra in Figure 3c show a distinct peak shift of ~0.3 eV in the binding energy for $4f_{7/2}$ and $4f_{5/2}$ toward lower values in $WO_3/NH_3/Fe$ compared to WO_3 (Figure 3a). This shift was observed for doping by atoms of lower valency, such as Fe^{2+}/Fe^{3+} substituting for W^{6+}.[51−53] The contribution from W^{5+} or other WO_x species, present only in $WO_3/NH_3/Fe$, is relatively weak compared to that of W^{6+} but suggests the presence of oxygen vacancies and supports the $WO_{2.92}$ phase detected by XRD. The deconvoluted O 1s spectra in Figure 3b show the contribution of lattice oxygen (~530 eV) and adsorbed oxygen (~532 eV) in WO_3. However, a significant contribution from oxygen vacancies or oxygen-deficient regions (~531 eV) is observed only in $WO_3/NH_3/Fe$, as shown in Figure 3d. The low binding energy component is directly related to the stoichiometry of the compound, while the high binding energy component arises from loosely bound oxygen, which cannot be entirely removed by annealing. Furthermore, the O 1s peak in $WO_3/NH_3/Fe$ is shifted by ~0.5 eV toward lower binding energies, suggesting possible Fe doping.[54,55] The deconvoluted Fe 2p spectra in Figure 3e confirm the presence of both Fe^{3+} and Fe^{2+} oxidation states along with their corresponding satellite peaks. The Fe $2p_{3/2}$ and $2p_{1/2}$ peaks are separated by ~14 eV, with an area ratio of about 2:1, as expected. The Fe^{3+} species may possibly originate from Fe_2WO_6, Fe_3O_4, or Fe_2O_3, while Fe^{2+} could be attributed to $FeWO_4$ and Fe_3O_4.[30] However, the XRD patterns specifically indicate the formation of $FeWO_4$ and Fe_3O_4.

The Raman spectra of $WO_3/NH_3/Fe$ and WO_3, shown in Figure 3f, reveal bands at 270, 323, 713, and 803 cm^{-1} that are characteristic of monoclinic WO_3 vibration modes. The first two bands correspond to O−W−O bending modes, while the next two are associated with O−W−O stretching modes.[56] A broad hump around 650 cm^{-1} may be attributed to the Fe_3O_4 phase in $WO_3/NH_3/Fe$, though it is not prominent due to the low amount of Fe, as suggested by the XRD data. The band at 713 cm^{-1} shifts by 3 cm^{-1} toward lower wavenumbers in $WO_3/NH_3/Fe$, as expected due to low Fe doping.[57] The band at 804 cm^{-1} shifts slightly further to 802.3 cm^{-1}, which is consistent with existing literature on Fe-doped WO_3.[50]

LSV curves (Figure 4a) were recorded for the optimized air-annealed $WO_3/NH_3/Fe$ sample, and presented alongside that from WO_3.[41] The $WO_3/NH_3/Fe$ sample demonstrated a photocurrent of up to 0.43 mA cm^{-2} at 1.23 V vs RHE, compared to 0.34 mA cm^{-2} for pristine WO_3. This is undoubtedly a result of doping of the semiconductor layer and the formation of new $FeWO_4$ and Fe_3O_4 phases on the surface of the anodic WO_3. The $WO_3/NH_3/Fe$ sample exhibited nearly double the photocurrent at lower biases (up to 1.0 V vs RHE) compared to WO_3, although WO_3 remained competitive at higher potentials. The performance comparison of these two with other samples prepared with slight variations in the synthesis route is provided in Figure S4 (Supporting Information) but is discussed here to understand better the causes behind the superiority of the best-performing material. In all of the data, the dark current was negligible across the entire potential range, indicating the absence of corrosion or significant electrocatalysis in 0.1 M Na_2SO_4. First, the effects of

https://doi.org/10.1021/acsami.5c03437
ACS Appl. Mater. Interfaces 2025, 17, 30284−30296

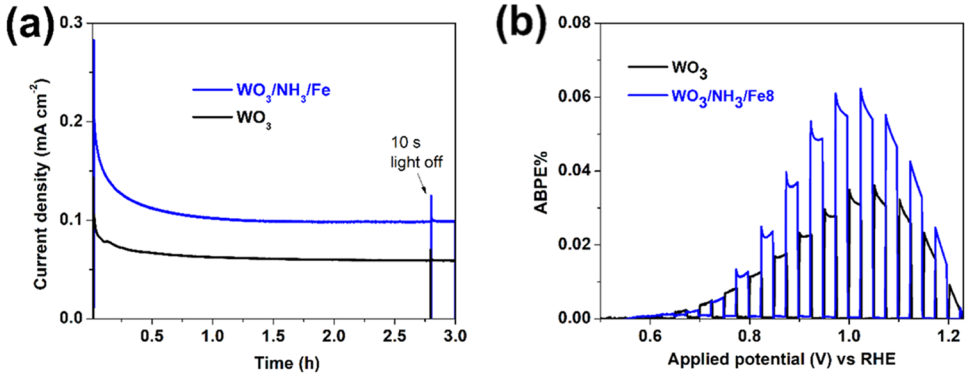

Figure 5. (a) Current vs time curves recorded at 1.0 V vs RHE, and (b) ABPE plots for WO_3 and $WO_3/NH_3/Fe$ materials.

varying the molarity of the overlayer precursor (0.063, 0.125, 0.25 mM Mohr's salt) are compared in Figure S4a (Supporting Information). The samples synthesized with very low molarity of 0.063 mM performed worse than pristine WO_3 at higher potentials possibly because the pH set by 25% NH_3 was insufficiently utilized by the Mohr's salt, increasing the likelihood of WO_3 surface corrosion. Also, a higher molarity of 0.25 mM resulted in low photocurrents in the entire potential window. Beyond its intended role in co-catalysis and light sensitization, a thicker low-band gap overlayer might have shaded the underlying WO_3 from UV light or introduced unfavorable deep defect levels, promoting charge trapping and recombination. Figure S4b (Supporting Information) demonstrates the effect of different Fe precursors, Fe(III) chloride and Fe(II) sulfate, on photocurrent, compared to the superior Mohr's salt at an equal concentration of 0.125 mM. This could be a direct result of the smaller particle sizes of the overlayer in the case of Mohr's salt. Figure S4c (Supporting Information) compares electrodes annealed in vacuum and air for equal duration and at the same temperature. Vacuum-annealed samples perform worse than their air-annealed counterparts but still showed better PEC activity than pure WO_3. These studies support the idea that an optimized thin co-catalyst layer is necessary to translate surface properties into higher photocurrent. On the other hand, an excessive amount of Fe compounds on the WO_3 surface ultimately have a negative impact on photocurrent in a system as this which requires front illumination. Additionally, a control electrode, where NH_3 was used to set the pH at 8 during hydrothermal treatment without adding Fe precursors, performed worse than pristine WO_3. This suggests that the observed photocurrent enhancement is not due to N doping by NH_3 (as confirmed by EDS, Figure 1f) and that alkaline media degrade WO_3 in the absence of other reactants. It is also observed that replacing NH_3 with NaOH to achieve the pH = 8 reaction medium (for 0.125 mM Mohr's salt) led to a severe deterioration in photocurrent, likely due to differences in reaction kinetics. Notably, the onset potentials remained similar, ruling out the contribution from improved visible light absorption as the primary cause of the higher photocurrent.

To further investigate the electron transfer mechanism, electrochemical impedance spectroscopy was performed. To eliminate the effect of minor differences in the electrode area, the data were normalized. The fitted Nyquist plots, under both dark and illuminated conditions, are presented in Figure 4b for WO_3 and $WO_3/NH_3/Fe$ at a potential (1.0 V vs RHE) significantly above the onset. At this potential, charge transfer occurs without the pronounced effects of radiative recombination, allowing for more reliable equivalent circuit fitting. The corresponding fitted Bode plots under illumination has also been provided in Figure 4c to highlight the goodness of fitting over the full frequency range investigated. Given as the inset of Figure 4b, the circuit (1) for porous WO_3 features a single R-C loop, whereas that of $WO_3/NH_3/Fe$ (2) exhibits an additional loop corresponding to the surface layer.[58] A Warburg impedance component is also included to account for diffusion effects and is supported by the low-frequency phase plot features observed for $WO_3/NH_3/Fe$ (Figure 4(d)). Under illumination, the charge trapping resistances for $WO_3/NH_3/Fe$ and WO_3 are lower than those under dark conditions. Smaller charge transfer resistance at the semiconductor/electrolyte interface, as estimated from the semicircular arc diameter, was observed for $WO_3/NH_3/Fe$. The equivalent circuit under illumination and relevant fitting parameters are summarized in Table S2 (Supporting Information). Notably, the interfacial charge transfer resistance ($R_{CTinterface}$) of pristine WO_3 under illumination decreased by 3.4 times with surface modification (i.e., for $WO_3/NH_3/Fe$) indicating improved charge separation and suppression of radiative electron−hole pair recombination. This happens due to the change of the chemical nature of the WO_3 surface by co-catalysts or by improving the conductivity and reducing ohmic resistance of the photoelectrode. The results suggest that the oxygen vacancy-rich $WO_3/NH_3/Fe$ surface has beneficial surface defects that can act as active catalytic sites for water oxidation.

The Bode phase plots recorded in the dark and under illumination for WO_3 and $WO_3/NH_3/Fe$ samples as presented in Figure 4d show that the frequency (f) of the prominent peak in the low-frequency range under illumination is lower for $WO_3/NH_3/Fe$ compared to WO_3. This low-frequency range corresponds to charge transfer at the semiconductor/electrolyte interface. The reduced frequency indicates a longer charge carrier lifetime ($\tau = 1/2\pi f$) for $WO_3/NH_3/Fe$. A longer charge carrier lifetime suppresses recombination, enhances separation efficiency, and consequently can contribute to a higher photocurrent. This improvement can likely be attributed to built-in internal electric field at the p-type $FeWO_4$/n-type Fe doped WO_3 heterojunction,[17] considering that the amount of the Fe_3O_4 phase detected is much less than $FeWO_4$.

The amperometric photoresponse of $WO_3/NH_3/Fe$ under 3 h of simulated solar illumination at 1.0 V vs RHE is shown in Figure 5a. The initial transient photoresponse spike quickly decays due to the competing effect of recombination and charge transfer but eventually stabilizes into a steady state for

https://doi.org/10.1021/acsami.5c03437
ACS Appl. Mater. Interfaces 2025, 17, 30284−30296

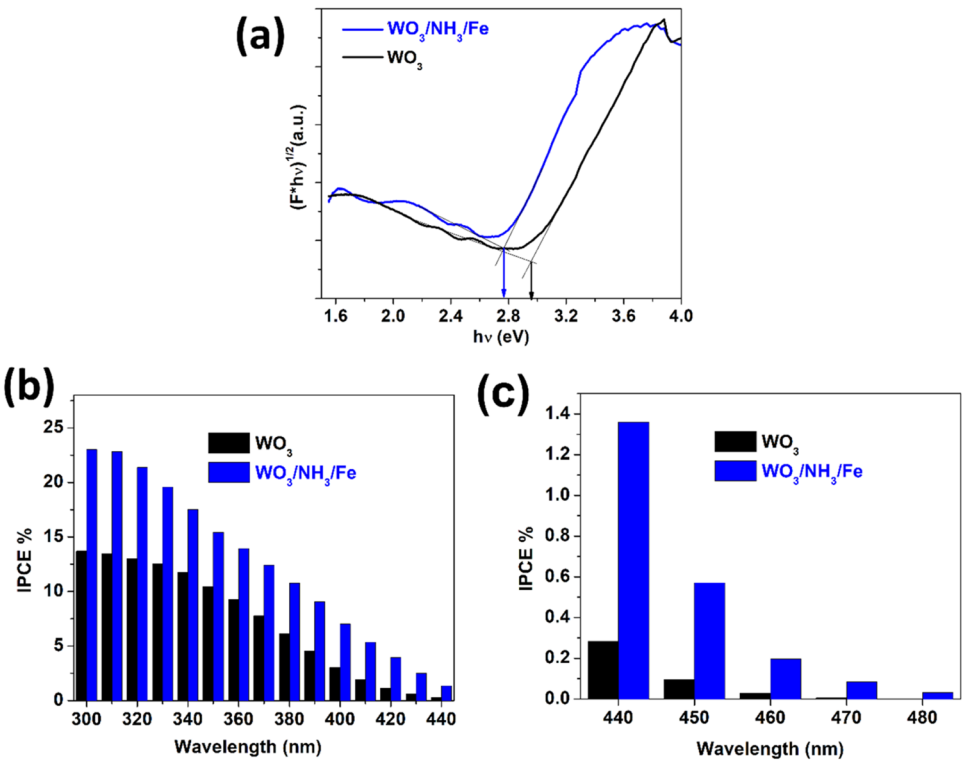

Figure 6. (a) Tauc plots derived from the Kubelka–Munk transformation of UV–Vis DRS data to determine the indirect band gap of WO_3 and $WO_3/NH_3/Fe$. (b-c) IPCE plots for WO_3 and $WO_3/NH_3/Fe$ at 1.2 V vs RHE for the (b) 300–440 and (c) 440–480 nm wavelength range.

both $WO_3/NH_3/Fe$ and WO_3. The steady-state photocurrent value at the end of the illumination period is 1.7 times higher for $WO_3/NH_3/Fe$ compared to WO_3, indicating greater potential for efficient long-term use. Various processes may occur during operation, such as the formation and degradation of peroxo- species, Na^+ intercalation/deintercalation, healing or expansion of surface defects (e.g., oxygen vacancies), oxide dissolution, and oxidation of the underlying W metal.[59−61] The prolonged performance tests indicate that an equilibrium is eventually established between detrimental photocorrosion and beneficial water oxidation activity. However, while hydrothermal treatment helps to maintain the stability of WO_3, it does not lead to a significant enhancement. Figure S4d (Supporting Information) presents current vs time curves recorded at a higher potential of 1.2 V vs RHE over a few minutes of illumination for $WO_3/NH_3/Fe$, $WO_3/NH_3/Fe$ (vac), $WO_3/NaOH/Fe$, WO_3/NH_3, and WO_3. Among these, even if optimized $WO_3/NH_3/Fe$ has the highest magnitude of photocurrent, stability is achieved quicker for $WO_3/NH_3/Fe$ (vac) possibly due to the protective role on WO_3 from having more $FeWO_4$ (as indicated by XRD peak intensity in Figure 2b). Figure S5 in Supporting Information presents the data for 30 min of illumination at 1.0 V vs RHE on a different batch of these two samples showing almost double photocurrent when stabilized. Figure 5b demonstrates the applied bias photon to current (ABPE) efficiency of $WO_3/NH_3/Fe$ in comparison to WO_3, assuming a negligible corrosion current and unity faradaic efficiency. The ABPE% was calculated using eq S5 detailed in Supporting Information. The efficiency nearly doubles at ∼0.9 V vs RHE, highlighting the promising utility of the modified photoanodes at low bias. Furthermore, we have studied the charge injection (surface charge separation) and bulk charge separation efficiencies following an established protocol reported in the literature, and the obtained results are presented in Figure S6a,b respectively.[62] Surface charge recombination is significantly suppressed in the presence of a hole scavenger such as Na_2SO_3, while bulk charge separation remains largely unaffected. Therefore, charge injection efficiency was calculated as the ratio of the photocurrent density for water oxidation in 0.1 M Na_2SO_4 to that obtained for sulfite oxidation in 0.1 M Na_2SO_4 containing 0.1 M Na_2SO_3. A higher photocurrent in the presence of sulfite compared with that in its absence indicates greater recombination loss before the photogenerated holes can participate in water oxidation. The $WO_3/NH_3/Fe$ electrode exhibits moderately improved charge injection efficiency compared to pristine WO_3, suggesting enhanced hole transfer from the electrode surface to the electrolyte. The calculation method for charge separation efficiency is provided as eq S6 in Supporting Information.[62] Notably, the efficiency of $WO_3/NH_3/Fe$ is higher and increases with applied potential, supporting conclusions drawn from impedance spectroscopy that the heterojunctions formed contribute to an internal electric field that facilitates faster electron–hole separation, thereby minimizing recombination and improving light energy utilization.

Figure 6a presents the Tauc plots derived from UV–Vis DRS, following the Kubelka–Munk transformation of the reflectance data.[40] The Tauc equation S7 used to plot and estimate the indirect band gaps has been described in the Supporting Information. The indirect band gaps of WO_3, and $WO_3/NH_3/Fe$ were found to be ∼2.96 and 2.77 eV, respectively. This indicates only a slight shift in the absorption edge, possibly due to VB (valence band maxima) coming closer to CB (conduction band minima) on Fe doping and the sensitization by low band gap phases (Fe_3O_4, $FeWO_4$),

https://doi.org/10.1021/acsami.5c03437
ACS Appl. Mater. Interfaces 2025, 17, 30284−30296

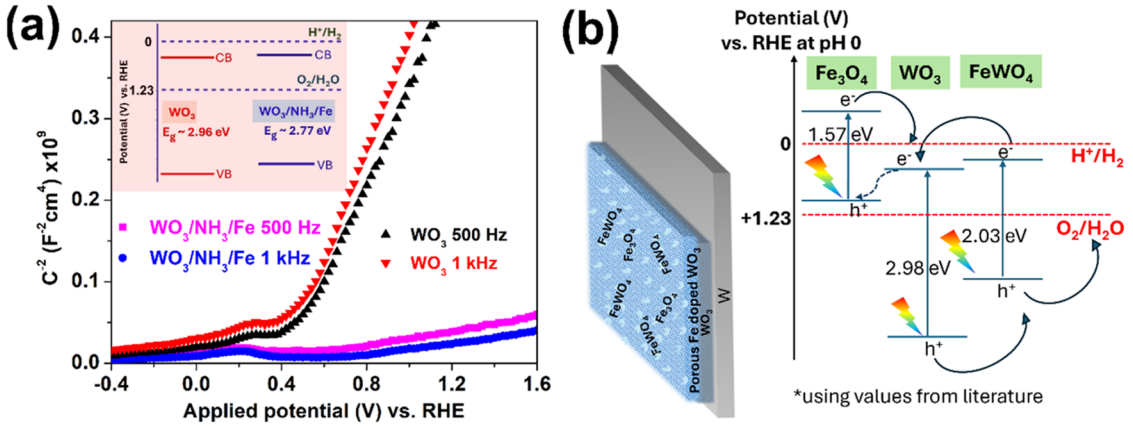

Figure 7. (a) Mott–Schottky plots for WO_3 and WO_3/NH_3/Fe at 500 and 1000 Hz, recorded in the dark and (inset) their approximately estimated conduction and valence band edges. (b) Schematic representation of the composition of WO_3/NH_3/Fe photoelectrode and a possible electron–hole separation and transfer mechanism for water oxidation under illumination.

contributing minimally to visible light absorption. Figure 6b,c demonstrates the IPCE plots in different wavelength ranges. The IPCE % has been calculated from photocurrent data using eq S8 described in Supporting Information. It is evident in Figure 6b that both WO_3 and WO_3/NH_3/Fe samples exhibit the highest conversion efficiency under ultraviolet light (~300 nm), with WO_3/NH_3/Fe significantly outperforming WO_3. Additionally, the IPCE% data in Figure 6c for 400–480 nm wavelength highlight a much higher performance for WO_3/NH_3/Fe compared to WO_3 under visible light. It is not only due to the lower optical band gap but also probably due to the reduced recombination of charge carriers probably. This is much better than existing report of electrodeposited Fe_2O_3 on anodic WO_3 and thus may suggest superiority of Fe doping and interfacing with $FeWO_4$ and Fe_3O_4 for anodic WO_3 sensitization over use of only Fe oxide cocatalysts.[38] This suggests that WO_3/NH_3/Fe has a better ability to utilize the visible range of the solar spectrum, pointing toward its applicability under visible light sources such as light emitting diodes (LEDs).

Additionally, impedance vs potential data were recorded in the dark, and the corresponding Mott–Schottky plots (C^{-2} vs potential) at fixed frequencies of 500 and 1000 Hz are shown in Figure 7a. The governing Mott–Schottky eq S9 is provided in the Supporting Information.[22] The flat band potential V_{fb} is around 0.4 V vs RHE across different frequencies for both the samples and is just below the onset potential (~0.5 V vs RHE) observed in the LSV curves as expected. The positive slopes of the linear portion of the Mott–Schottky plots for both WO_3 and WO_3/NH_3/Fe confirm the predominantly n-type semiconductor nature of the primary WO_3 material. The slope (m) of the linear portion of the plot is indirectly proportional to the value of donor density N_D.[40] The N_D for WO_3 is therefore significantly lower than that for WO_3/NH_3/Fe, as evident from the steep slope and correlated to literature report of Fe-doped WO_3.[52] This increased donor concentration which may contribute to enhanced catalytic activity could arise from the observed oxygen vacancies[54] on aliovalent doping and built-in electric field at the heterojunction.[63] Surface oxygen vacancies created in WO_3 can facilitate water molecule adsorption, potentially enhancing the water oxidation kinetics. However, these vacancies can also localize charge carriers, reducing electronic conductivity and promoting recombination of photogenerated holes before they contribute to the desired reaction. Introducing transition metal dopants like Fe can mitigate these issues. The nonlocalized 3d orbitals of Fe may passivate low-energy defect traps, improving charge transport. Additionally, the Fe dopant and $FeWO_4$ co-catalyst can passivate intrinsic surface/bulk defects commonly present in anodic tungsten oxide (which is generally non-stoichiometric), thereby enhancing photoelectrochemical performance. Post-hydrothermal annealing is crucial for achieving high crystallinity, which further reduces the defect density. However, excessive doping can block active sites, underscoring the importance of optimizing Fe precursor concentrations.[60] Our studies have shown that varying Fe precursors (of the same molarity) and altering annealing atmospheres (vacuum vs air) at the same temperatures can lead to differences in photoelectrochemical behavior due to variation in doping levels and cocatalyst formation. This highlights the necessity of carefully designing heterojunctions to maximize the benefits while minimizing potential drawbacks. The inset shows the CB and VB as estimated from their flat band potentials (which approximately indicate CB for an n-type semiconductor) and by using band gap values derived from the Tauc plot. The CB and VB levels after surface modification are raised compared to that of WO_3 which is possibly a combined result of Fe doped WO_3 and Fe_3O_4–$FeWO_4$ phase formation along with WO_3. A similar trend is observed in the valence band spectra obtained during XPS measurement, as shown in Figure S7, indicating that the VB maximum of WO_3/NH_3/Fe is positioned ~ 0.7 eV higher than that of pristine WO_3. But both of these level estimations include the effect of W substrate and also the primary WO_3 in case of the overlayer. Therefore, the mechanism of electron transfer at Fe_3O_4–$FeWO_4$/Fe doped WO_3 heterojunction under illumination may be better visualized with band diagram constructed using values for pure WO_3, $FeWO_4$ and Fe_3O_4 taken from literature[35,64] and presented in Figure 7b. The Fe doping is very low, and therefore, although the VB level should be raised slightly (<0.2 eV, as UV-VisDRS suggests) compared to pure oxide, the values for pure WO_3 have been used here for mechanistic insight. Electron–hole pairs are created in these semiconductors upon light irradiation of wavelengths smaller than their absorption edge. Low band gap Fe_3O_4 may act as a light sensitizer by injecting electrons to the CB of WO_3. However, it can also create a recombination pathway (dotted line) for electrons to recombine with holes in the VB of Fe_3O_4 (which is

https://doi.org/10.1021/acsami.5c03437
ACS Appl. Mater. Interfaces 2025, 17, 30284–30296

not at a favorable energy level for water oxidation) and in best case, this could help in Z-scheme charge separation.[65] The undesired recombination can be mitigated if electrons transfer efficiently from the photoanode to the cathode via the W substrate. To achieve this, employing a direct in situ growth method on the WO_3 electrode facilitates improved interfacial contact and lattice matching with the tungstate overlayer. The hydrothermal process concurrently introduces Fe dopants into the WO_3 layer, where unsaturated d orbitals of Fe can provide intermediate energy levels, enhancing charge transfer. Notably, wet-chemical doping directly on WO_3 electrodes can result in a gradient doping profile due to the element diffusion,[66] which aids in efficient electron transport through multiple energy steps. The doping in metal oxide like WO_3 induces the formation of oxygen vacancies, which act as donor states, increasing carrier density and leading to enhanced band bending at the semiconductor/electrolyte interface. This band bending is crucial for efficient charge separation, as it creates an internal electric field that drives photogenerated charge carriers toward the respective electrodes, thereby improving photoelectrochemical performance. Additionally, it is to be noted that the crystalline Fe_3O_4 phase likely plays a minimal role in this process due to its relatively low quantity, as indicated by XRD analysis. The VB levels of WO_3 and $FeWO_4$ are favorably below the water oxidation potential just like the operation as a water splitting photoanode demands. The step like heterojunction (type II) forming between WO_3 and $FeWO_4$ helps to prevent recombination by quick charge separation.[16] The electrons are transferred from higher to lower CB (WO_3) and the holes are transferred from lower to higher VB ($FeWO_4$), from where the electrons can go to external circuit via substrate to cathode for water reduction, and the holes can take part in water oxidation.

In general, the performance of photoelectrodes is highly dependent on the synthesis procedure. Numerous studies[29,67−69] have investigated Fe-based overlayers on WO_3 electrodes synthesized via various methods (Table S3, Supporting Information). Most of these reports demonstrate a photocurrent enhancement comparable to that observed in this work and typically involve multistep procedures based on a transparent substrate, unlike the opaque W substrate used here, which is designed for back illumination. However, there are only a few reports of anodically grown WO_3 photoanodes with various overlayers/modifications for enhanced photoelectrochemical (PEC) water oxidation.[23,38,40,41,70] A comparative analysis of these studies is presented in Table S4 (Supporting Information).

4. CONCLUSIONS

We have successfully developed porous tungsten oxide-based photoelectrodes by using the reproducible technique of anodic tungsten oxidation, followed by a hydrothermal treatment. This resulted in the simultaneous formation of a thin iron tungstate/magnetite based layer on WO_3 along with doping of WO_3 with iron. This study is one of the few works devoted to anodized WO_3 photoelectrodes with overlayers and may inspire future research utilizing such opaque conducting substrates, where light cannot be incident through the WO_3 side. A slow yet straightforward hydrothermal reaction enables moderately scalable engineering of the crystalline phase on primary electrodes, offering considerable purity and size control at moderate temperatures. However, the vigorous reaction in a liquid medium may damage the primary electrode. Nevertheless, we could find suitable parameters of the one-step hydrothermal engineering of anodic WO_3 surface with iron based precursor which is critical for applicability as an improved stable photoelectrode under front illumination. Stable photocurrent densities at low bias under simulated solar light were nearly double those of the pristine WO_3 electrodes. The bang gap change was minimal, and the onset potential remained largely unchanged. Therefore, the observed performance enhancement can be attributed to increased donor density, the presence of oxygen vacancies, and improved charge transfer efficiency due to reduced recombination at the heterojunction. The modifications to WO_3 also resulted in considerably higher incident photon-to-current conversion efficiencies under visible light, although the improvements were less pronounced in the ultraviolet region. Nonetheless, this method offers a scalable and cost-effective approach to addressing recombination issues in anodized WO_3 photoelectrodes.

■ ASSOCIATED CONTENT

Data Availability Statement

The data presented in this study are available at RODBUK Cracow Open Research Data Repository at https://doi.org/10.57903/UJ/X9Y5BR

Supporting Information

The Supporting Information is available free of charge at https://pubs.acs.org/doi/10.1021/acsami.5c03437.

Schematic of the optimized route for electrode fabrication, all of the equations used to plot the graphs and explain the results; comprehensive table with details of other samples presented for optimization; FESEM top view image of all samples for optimization except the optimized $WO_3/NH_3/Fe$ and WO_3; LSV curves for these samples, amperometric curves (at 1.2 V vs RHE and 1.0 V vs RHE) for selected samples; charge separation and injection efficiency plots for $WO_3/NH_3/Fe$ and WO_3; XPS valence band spectra of $WO_3/NH_3/Fe$ and WO3; performance comparison tables with relevant studies on modified anodic WO_3 and Fe-modified WO_3 photoanodes (PDF)

■ AUTHOR INFORMATION

Corresponding Authors

Piyali Chatterjee − *Department of Physical Chemistry and Electrochemistry, Faculty of Chemistry, Jagiellonian University, 30-387 Krakow, Poland;* orcid.org/0000-0003-4259-0267; Email: piyali93physics@gmail.com, piyali.chatterjee@uj.edu.pl

Grzegorz D. Sulka − *Department of Physical Chemistry and Electrochemistry, Faculty of Chemistry, Jagiellonian University, 30-387 Krakow, Poland;* orcid.org/0000-0001-7431-617X; Email: sulka@chemia.uj.edu.pl

Authors

Daniel Piecha − *Department of Physical Chemistry and Electrochemistry, Faculty of Chemistry, Jagiellonian University, 30-387 Krakow, Poland; Doctoral School of Exact and Natural Sciences, Jagiellonian University, 30-348 Krakow, Poland;* orcid.org/0009-0004-3099-4920

Sebastian Kotarba − *Department of Physical Chemistry and Electrochemistry, Faculty of Chemistry, Jagiellonian University, 30-387 Krakow, Poland*

Karolina Syrek − *Department of Physical Chemistry and Electrochemistry, Faculty of Chemistry, Jagiellonian University, 30-387 Krakow, Poland;* orcid.org/0000-0002-4041-9100

Marcin Pisarek − *Laboratory of Surface Analysis, Institute of Physical Chemistry, Polish Academy of Sciences, Warsaw 01-224, Poland;* orcid.org/0000-0002-7424-5954

Complete contact information is available at: https://pubs.acs.org/10.1021/acsami.5c03437

Notes

The authors declare no competing financial interest.

■ ACKNOWLEDGMENTS

This research is part of the POLONEZ BIS 3 project No. 2022/47/P/ST5/00813 cofunded by the National Science Center and the European Union Framework Program for Research and Innovation Horizon 2020 under the Marie Skłodowska-Curie grant agreement no. 945339. The study was carried out using research infrastructure funded by the European Union in the framework of the Smart Growth Operational Program, Measure 4.2; Grant No. POIR.04.02.00-00-D001/20, "ATOMIN 2.0 − Center for materials research on ATOMic scale for the INnovative economy." The FESEM imaging was performed in the Laboratory of Field Emission Scanning Electron Microscopy and Microanalysis at the Institute of Geological Sciences, Jagiellonian University, Poland.

■ REFERENCES

(1) Zhao, Y.; Niu, Z.; Zhao, J.; Xue, L.; Fu, X.; Long, J. Recent advancements in photoelectrochemical water splitting for hydrogen production. *Electrochem. Energy Rev.* **2023**, *6*, No. 14, DOI: 10.1007/s41918-022-00153-7.

(2) Fujishima, A.; Honda, K. Electrochemical photolysis of water at a semiconductor electrode. *Nature* **1972**, *238* (5358), 37−38.

(3) Costa, M. B.; de, A.; Marcos; Juliana; Mascaro, L. H. Current Trending and beyond for solar-driven water splitting reaction on WO_3 photoanodes. *J. Energy Chem.* **2022**, *73*, 88−113.

(4) Li, Y.; Liu, Z.; Guo, Z.; Ruan, M.; Li, X.; Liu, Y. Efficient WO_3 photoanode modified by Pt layer and plasmonic Ag for enhanced charge separation and transfer to promote photoelectrochemical performances. *ACS Sustainable Chem. Eng.* **2019**, *7* (14), 12582−12590.

(5) Yan, L.; Dong, G.; Huang, X.; Zhang, Y.; Bi, Y. Unraveling oxygen vacancy changes of WO_3 photoanodes for promoting oxygen evolution reaction. *Appl. Catal., B* **2024**, *345*, No. 123682.

(6) Gelija, D.; Loka, C.; Goddati, M.; Bak, N.; Lee, J.; Kim, M.-D. Integration of Ag plasmonic metal and WO_3/InGaN heterostructure for photoelectrochemical water splitting. *ACS Appl. Mater. Interfaces* **2023**, *15* (29), 34883−34894.

(7) Htet, H.T.; Jung, Y.; Kim, Y.; Lee, S. Enhanced photoelectrochemical water splitting using $NiMoO_4$/$BiVO_4$/Sn-doped WO_3 double heterojunction photoanodes. *ACS Appl. Mater. Interfaces* **2024**, *16* (39), 52383−52392.

(8) Ma, Y.; Hu, Y. H. Surface-copper-doped WO_3 photoanode for photoelectrochemical water splitting. *Appl. Phys. Lett.* **2021**, *118* (22), No. 223903.

(9) Wattanawikkam, C.; Bootchanont, A.; Porjai, P.; Jetjamnong, C.; Kowong, R.; Lertvanithphol, T.; Chananonnawathorn, C.; Chirawatkul, P.; Chanlek, N.; Nakajima, H.; Songsiriritthigul, P.; Kiama, N.; Nareejun, W.; Tomkham, P.; Ponchio, C.; Rahong, S.; Klamchuen, A.; Horprathum, M. Phase evolution in annealed Ni-doped WO_3 nanorod films prepared via a glancing angle deposition technique for enhanced photoelectrochemical performance. *Appl. Surf. Sci.* **2022**, *584*, No. 152581.

(10) Xie, Z.; Chen, D.; Zhai, J.; Huang, Y.; Ji, H. Charge separation via synergy of homojunction and electrocatalyst in $BiVO_4$ for photoelectrochemical water splitting. *Appl. Catal., B* **2023**, *334*, 122865.

(11) Zhang, B.; Tang, Y.; Wu, X.; Xie, H.; Zhao, F.; Zeng, B. Experimental and DFT studies of novel Z-scheme Bi-doped Bi_2WO_6/Bi_2S_3 p-n/n homo/heterojunction and its application in cathodic photoelectrochemical immunosensing. *Sens. Actuators, B* **2021**, *346*, 130455.

(12) Gao, Y.; Zeng, Y.; Liu, X.; Tang, D. Liposome-mediated *in situ* formation of type-I heterojunction for amplified photoelectrochemical immunoassay. *Anal. Chem.* **2022**, *94* (11), 4859−4865.

(13) Lee, J.; Son, N.; Shin, H.; Kim, J.; Park, N.-K.; Kim, U. S.; Kang, M. An eco-efficient dual-function technology: Magnetically recoverable RGO-WO_3/Fe_3O_4 ternary heterojunction catalytic system simultaneously performing malachite green photolysis and Cr(VI) reduction. *J. Cleaner Prod.* **2024**, *459*, 142533.

(14) Pirsaheb, M.; Hossaini, H.; Fatahi, N.; Jafari, Z.; Jafari, F.; Motlagh, R. J. Photocatalytic removal of organophosphorus pesticide by the WO_3-Fe_3O_4/RGO photocatalyst under visible light. *Environ. Sci. Pollut. Res.* **2024**, *31* (2), 2555−2568.

(15) Yu, Z.; Xu, J.; Li, Y.; Gong, H.; Wei, Q.; Tang, D. Ferroelectric perovskite-enhanced photoelectrochemical immunoassay with the photoexcited charge-transfer of a built-in electric field. *J. Mater. Chem. C* **2021**, *9* (40), 14351−14358.

(16) Murugan, C.; Mary, A. S.; Velmurugan, R.; Subramanian, B.; Murugan, P.; Pandikumar, A. Investigating the interfacial charge transfer between electrodeposited $BiVO_4$ and pulsed laser-deposited Co_3O_4 p−n junction photoanode in photoelectrocatalytic water splitting. *Chem. Eng. J.* **2024**, *483*, 149104.

(17) Li, J.; Meng, F.; Suri, S.; Ding, W.; Huang, F.; Wu, N. Photoelectrochemical performance enhanced by a nickel oxide−hematite p−n junction photoanode. *Chem. Commun.* **2012**, *48* (66), 8213−8215.

(18) Ahmed, M. G.; Kandiel, T. A.; Ahmed, A. Y.; Kretschmer, I.; Rashwan, F. A.; Bahnemann, D. W. Enhanced photoelectrochemical water oxidation on nanostructured hematite photoanodes via p-$CaFe_2O_4$/n-Fe_2O_3 heterojunction formation. *J. Phys. Chem. C* **2015**, *119* (11), 5864−5871.

(19) Liu, Z.; Song, Q.; Zhou, M.; Guo, Z.; Kang, J.; Yan, H. Synergistic enhancement of charge management and surface reaction kinetics by spatially separated cocatalysts and p-n heterojunctions in Pt/$CuWO_4$/Co_3O_4 photoanode. *Chem. Eng. J.* **2019**, *374*, 554−563.

(20) Jin, W.; Zhang, R.; Chen, J.; Sun, H.; Xia, W.; He, J.; Zeng, X. An optimized Fe_3O_4/Fe_2O_3 pn junction photoelectrode with multiscale structure and broad spectrum absorption. *Sol. Energy Mater. Sol Cells* **2023**, *254*, No. 112287.

(21) Zhu, J.; Li, W.; Li, J.; Li, Y.; Hu, H.; Yang, Y. Photoelectrochemical activity of $NiWO_4$/WO_3 heterojunction photoanode under visible light irradiation. *Electrochim. Acta* **2013**, *112*, 191−198.

(22) Chatterjee, P.; Chakraborty, A. K. Enhanced solar water oxidation by $CoWO_4$-WO_3 heterojunction photoanode. *Sol. Energy* **2022**, *232*, 312−319.

(23) Zych, M.; Syrek, K.; Wiercigroch, E.; Malek, K.; Kozieł, M.; Sulka, G. D. Visible-light sensitization of anodic tungsten oxide layers with $CuWO_4$. *Electrochim. Acta* **2021**, *368*, No. 137591.

(24) Zhang, H.; Tian, W.; Li, Y.; Sun, H.; Tadé, M. O.; Wang, S. Heterostructured WO_3@$CoWO_4$ bilayer nanosheets for enhanced visible-light photo, electro and photoelectro-chemical oxidation of water. *J. Mater. Chem. A* **2018**, *6* (15), 6265−6272.

(25) Zhu, T.; Chong, M. N.; Chan, E. S.; Ocon, J. D. Electrochemically-synthesized tungstate nanocomposites γ-WO_3/$CuWO_4$ and γ-WO_3/$NiWO_4$ thin films with improved band gap and photoactivity for solar-driven photoelectrochemical water oxidation. *J. Alloys Compd.* **2018**, *762*, 90−97.

(26) Escaliante, L. C.; Azevedo, F.; Mendoza, H. E.; Xiao, C.; Kandel, R.; Humberto, J.; Osterloh, F. E. Sputter-coated TiO_2 films as

passivation and hole transfer layers for improved energy conversion with solar fuel WO_3/$CuWO_4$ photoanodes. *ACS Appl. Mater. Interfaces* **2024**, *16* (50), 69229−69238.
(27) Loka, C.; Gelija, D.; Prabhakar, V.; Lee, K.-S. Silver-boosted WO_3/$CuWO_4$ heterojunction thin films for enhanced photoelectrochemical water splitting efficiency. *ACS Sustainable Chem. Eng.* **2023**, *11* (32), 11978−11990.
(28) Li, J.; Hu, S.; Liu, S.; Hou, S.; Li, L.; Huang, J. In situ fabrication of WO_3/$CuWO_4$/CuO heterojunction photoanode for boosted interfacial charge transfer and enhanced photoelectrochemical water splitting. *Int. J. Hydrogen Energy* **2024**, *61*, 967−974.
(29) Lin, H.; Long, X.; An, Y.; Yang, S. *In situ* growth of Fe_2WO_6 on WO_3 nanosheets to fabricate heterojunction arrays for boosting solar water splitting. *J. Chem. Phys.* **2020**, *152* (21), No. 214704.
(30) Wang, H.; Wang, C.; Cui, X.; Qin, L.; Ding, R.; Wang, L.; Liu, Z.; Zheng, Z.; Baoliang, Lv. Design and facile one-step synthesis of $FeWO_4$/Fe_2O_3 di-modified WO_3 with super high photocatalytic activity toward degradation of quasi-phenothiazine dyes. *Appl. Catal., B* **2018**, *221*, 169−178.
(31) Liu, C.; Lü, H.; Yu, C.; Ding, B.; Ye, R.; Ji, Y.; Dai, B.; Liu, W. Novel $FeWO_4$/WO_3 nanoplate with p−n heterostructure and its enhanced mechanism for organic pollutants removal under visible-light illumination. *J. Environ. Chem. Eng.* **2020**, *8* (5), No. 104044.
(32) Chai, Q.; Dong, J.; Yu, X.; Zhang, X.; Li, J.; Guo, S.; Yang, Y. Photocatalytic activation of oxalic acid over FeOOH loaded $FeWO_4$/WO_3 heterojunction for high-efficient degradation of tetracycline. *J. Environ. Chem. Eng.* **2024**, *12* (1), No. 111728.
(33) Wang, X.; Ma, Q.; Wang, Y.; Zhao, D.; Li, L.; Zhang, H.; Li, B. MIL-101-derived porous WO_3/$FeWO_4$ hierarchical structures with efficient heterojunction interfaces for excellent room temperature n-butanol-sensing performance. *Chem. Eng. J.* **2024**, *479*, No. 147647.
(34) Kato, K.; Warsani, N. K. S. A.; Xin, Y.; Xu, Y.; Shirai, T. Ultrafast synthesis of WO_2−$W_{18}O_{49}$/$FeWO_4$ composites for near-infrared driven photocatalysis. *J. Alloys Compd.* **2024**, *991*, No. 174526.
(35) Huang, B.; Hart, J. N. DFT Study of various tungstates for photocatalytic water splitting. *Phys. Chem. Chem. Phys.* **2020**, *22* (3), 1727−1737.
(36) Adak, M.K.; Rajput, A.; Mallick, L.; Chakraborty, B. Electrochemically robust ferberite ($FeWO_4$) nanostructure as an anode material for alkaline water- and alcohol-oxidation reaction. *ACS Appl. Energy Mater.* **2022**, *5* (5), 5652−5665.
(37) Cristino, V.; Caramori, S.; Argazzi, R.; Meda, L.; Marra, G. L.; Bignozzi, C. A. Efficient photoelectrochemical water splitting by anodically grown WO_3 electrodes. *Langmuir* **2011**, *27* (11), 7276−7284.
(38) Zych, M.; Syrek, K.; Pisarek, M.; Sulka, G. D. Anodic WO_3 layers sensitized with hematite operating under the visible light spectrum. *J. Power Sources* **2022**, *541*, No. 231656.
(39) Berger, S. P.; Tsuchiya, H.; Ghicov, A.; Schmuki, P. High photocurrent conversion efficiency in self-organized porous WO_3. *Appl. Phys. Lett.* **2006**, *88* (20), No. 203119.
(40) Syrek, K.; Kotarba, S.; Zych, M.; Pisarek, M.; Uchacz, T.; Sobańska, K.; Pięta, Ł.; Sulka, G. D. Surface engineering of anodic WO_3 layers by in situ doping for light-assisted water splitting. *ACS Appl. Mater. Interfaces* **2024**, *16* (28), 36752−36762.
(41) Park, E.; Yoo, J.; Lee, K. Enhanced photoelectrochemical hydrogen production *via* linked $BiVO_4$ nanoparticles on anodic WO_3 nanocoral structures. *Sustainable Energy Fuels* **2024**, *8* (7), 1448−1456.
(42) Gonçalves, S.; Quitério, P.; Freitas, J.; Ivanou, D.; Lopes, T.; Mendes, A.; Araújo, J. P.; Sousa, C. T.; Apolinário, A. Unveiling morphology−structure interplay on hydrothermal WO_3 nanoplatelets for photoelectrochemical solar water splitting. *ACS Appl. Mater. Interfaces* **2024**, *16* (47), 64389−64409.
(43) Chen, X.; Ruan, M.; Wang, C.; Zhong, T.; Liu, Z. Phase engineering to construct In_2S_3 heterophase junctions and abundant active boundaries and surfaces for efficient pyro-PEC performance in CdS/In_2S_3. *J. Mater. Chem. A* **2024**, *12* (25), 15440−15452.
(44) Gao, Y.; Li, M.; Zeng, Y.; Liu, X.; Tang, D. Tunable competitive absorption-induced signal-on photoelectrochemical immunoassay for cardiac Troponin I based on Z-scheme metal−organic framework heterojunctions. *Anal. Chem.* **2022**, *94* (39), 13582−13589.
(45) Syrek, K.; Zych, M.; Zaraska, L.; Sulka, G. D. Influence of annealing conditions on anodic tungsten oxide layers and their photoelectrochemical activity. *Electrochim. Acta* **2017**, *231*, 61−68.
(46) Zhang, M.; Yang, C.; Zhang, Z.; Tian, W.; Hui, B.; Zhang, J.; Zhang, K. Tungsten oxide polymorphs and their multifunctional applications. *Adv. Colloid Interface Sci.* **2022**, *300*, No. 102596.
(47) Luxmi, V.; Kumar, A. Enhanced photocatalytic performance of M-WO_3 and M-Fe-doped WO_3 cuboids synthesized via sol-gel approach using egg albumen as a solvent. *Mater. Sci. Semicond. Process.* **2019**, *104*, 104690.
(48) Yousefi, R.; Zak, A. K.; Jamali-Sheini, F. Growth, X-ray peak broadening studies, and optical properties of Mg-doped ZnO nanoparticles. *Mater. Sci. Semicond. Process.* **2013**, *16* (3), 771−777.
(49) Khlifi, N.; Mnif, S.; Ben Nasr, F.; Fourati, N.; Zerrouki, C.; Chehimi, M. M.; Guermazi, H.; Aifa, S.; Guermazi, S. Non-doped and transition metal-doped CuO nano-powders: structure-physical properties and anti-adhesion activity relationship. *RSC Adv.* **2022**, *12* (36), 23527−23543.
(50) Tesfamichael, T.; Piloto, C.; Arita, M.; Bell, J. Fabrication of Fe-doped WO_3 films for NO_2 sensing at lower operating temperature. *Sens. Actuators B* **2015**, *221*, 393−400.
(51) Bathe, S. R.; Patil, P. S. Influence of Nb doping on the electrochromic properties of WO_3 films. *J. Phys. D* **2007**, *40* (23), 7423−7431.
(52) Zhang, T.; Chueh, C.-C.; Chen, H.; Bai, Y.; Xiao, S.; Xu, Q.; Xue, Q.; Yang, S. Iron-doping-enhanced photoelectrochemical water splitting performance of nanostructured WO_3: a combined experimental and theoretical study. *Nanoscale* **2015**, *7*, 2933−2940.
(53) Yang, Y.; Zhan, F.; Li, H.; Liu, W.; Yu, S. In situ Sn-doped WO_3 films with enhanced photoelectrochemical performance for reducing CO_2 into formic acid. *J. Solid State Electrochem.* **2017**, *21*, 2231−2240.
(54) Zhan, F.; Liu, Y.; Wang, K.; Liu, Y.; Yang, X.; Yang, Y.; Qiu, X.; Li, W.; Li, J. In situ formation of WO_3-based heterojunction photoanodes with abundant oxygen vacancies via a novel microbattery method. *ACS Appl. Mater. Interfaces* **2019**, *11* (17), 15467−15477.
(55) Chen, M.; Wang, X.; Yu, Y. H.; Pei, Z. L.; Bai, X. D.; Sun, C.; Huang, R. F.; Wen, L. S. X-ray photoelectron spectroscopy and Auger electron spectroscopy studies of Al-doped ZnO films. *Appl. Surf. Sci.* **2000**, *158* (1−2), 134−140.
(56) Diego-Lopez, A.; Cabezuelo, O.; Vidal-Moya, A.; Marin, M. L.; Bosca, F. Synthesis and mechanistic insights of SiO_2@WO_3@Fe_3O_4 as a novel supported photocatalyst for wastewater remediation under visible light. *Appl. Mater. Today* **2023**, *33*, 101879.
(57) Song, H.; Li, Y.; Lou, Z.; Xiao, M.; Hu, L.; Ye, Z.; Zeng, H. Synthesis of Fe-doped WO_3 nanostructures with high visible-light-driven photocatalytic activities. *Appl. Catal., B* **2015**, *166−167*, 112−120.
(58) Bredar, A. R. C.; Chown, A. L.; Burton, A. R.; Farnum, B. H. Electrochemical impedance spectroscopy of metal oxide electrodes for energy applications. *ACS Appl. Energy Mater.* **2020**, *3* (1), 66−98.
(59) Parvin, M.; Savickaja, I.; Tutliene, S.; Naujokaitis, A.; Ramanauskas, R.; Petruleviciene, M.; Juodkazyte, J. Nanostructured porous WO_3 for photoelectrochemical splitting of seawater. *J. Electroanal. Chem.* **2024**, *954*, No. 118026.
(60) Huang, Y.; Meng, L.; Xu, W.; Li, L. The positive versus negative effects of defect engineering for solar water splitting: a review. *Adv. Funct. Mater.* **2023**, *33* (47), No. 2305940.
(61) Szkoda, M.; Trzciński, K.; Trykowski, G.; Łapiński, M.; Lisowska-Oleksiak, A. Influence of alkali metal cations on the photoactivity of crystalline and exfoliated amorphous WO_3 − photointercalation phenomenon. *Appl. Catal., B* **2021**, *298*, 120527.
(62) Zhang, H.; Zhang, B.; Wang, X.; Zou, L.; You, J.; Lin, S. Effective charge separation in photoelectrochemical water splitting: a

https://doi.org/10.1021/acsami.5c03437
ACS Appl. Mater. Interfaces 2025, 17, 30284−30296

review from advanced evaluation methods to materials design. *Sustainable Energy Fuels* **2024**, *8* (11), 2357−2382.
(63) Chen, T.; Yang, C.; Rajendran, S.; Sawangphruk, M.; Zhang, X.; Qin, J. Utilizing the built-in electric field of p-n heterojunction to spatially separate the photogenerated charges in C, N co-doped Co_3O_4/CdS photocatalysts. *Fuel* **2023**, *331*, No. 125594.
(64) Elshypany, R.; Selim, H.; Zakaria, K.; Moustafa, A. H.; Sadeek, S. A.; Sharaa, S. I.; Raynaud, P.; Nada, A. A. Elaboration of Fe_3O_4/ZnO nanocomposite with highly performance photocatalytic activity for degradation methylene blue under visible light irradiation. *Environ. Technol. Innovation* **2021**, *23*, No. 101710.
(65) Zhang, L.; Luo, Z.; Zeng, R.; Zhou, Q.; Tang, D. All-solid-state metal-mediated Z-scheme photoelectrochemical immunoassay with enhanced photoexcited charge-separation for monitoring of prostate-specific antigen. *Biosens. Bioelectron.* **2019**, *134*, 1−7.
(66) Zhang, H.; Li, D.; Byun, W. J.; et al. Gradient tantalum-doped hematite homojunction photoanode improves both photocurrents and turn-on voltage for solar water splitting. *Nat. Commun.* **2020**, *11*, No. 4622.
(67) Zheng, G.; Jiang, S.; Cai, M.; Zhang, F.; Yu, H. WO_3/FeOOH Heterojunction for improved charge carrier separation and efficient photoelectrochemical water splitting. *J. Alloys Compd.* **2024**, *981*, 173637.
(68) Zhang, J.; Zhu, G.; Liu, W.; Xi, Y.; Golosov, D. A.; Zavadski, S. M.; Melnikov, S. N. 3D core-shell WO_3@α-Fe_2O_3 photoanode modified by ultrathin FeOOH layer for enhanced photoelectrochemical performances. *J. Alloys Compd.* **2020**, *834*, No. 154992.
(69) Chatterjee, P.; Chakraborty, A. K. Enhanced photoelectrochemical water oxidation by Fe(II) modified nanostructured WO_3 photoanode. *Opt. Mater.* **2023**, *144*, No. 114361.
(70) Levinas, R.; Tsyntsaru, N.; Cesiulis, H.; Viter, R.; Grundsteins, K.; Tamašauskaitė-Tamašiūnaitė, L.; Norkus, E. Electrochemical synthesis of a WO_3/MoS_x heterostructured bifunctional catalyst for efficient overall water splitting. *Coatings* **2023**, *13* (4), No. 673.

https://doi.org/10.1021/acsami.5c03437
ACS Appl. Mater. Interfaces 2025, 17, 30284−30296